Chinese Chemical Letters 33 (2022) 3752–3756

Contents lists available at ScienceDirect

Chinese Chemical Letters

journal homepage: www.elsevier.com/locate/cclet

Phase-mediated cobalt phosphide with unique core-shell architecture serving as efficient and bifunctional electrocatalyst for hydrogen evolution and oxygen reduction reaction

Junsheng Chen[a], Jianfeng Huang[a,*], Hai Wang[a], Weihang Feng[a], Tianmi Luo[a], Yuzhu Hu[a], Chengke Yuan[a], Liyun Cao[a,*], Yanni Jie[a], Koji Kajiyoshi[b], Yongqiang Feng[a,*]

[a] *School of Material Science and Engineering, International S&T Cooperation Foundation of Shaanxi Province, Xi'an Key Laboratory of Green Manufacture of Ceramic Materials, Shaanxi University of Science and Technology, Xi'an 710021, China*
[b] *Kochi University, Research Laboratory of Hydrothermal Chemistry, Kochi 780-8520, Japan*

ARTICLE INFO

Article history:
Received 26 September 2021
Revised 30 October 2021
Accepted 20 November 2021
Available online 25 November 2021

Keywords:
Electrocatalyst
Hydrogen evolution reaction
Oxygen reduction reaction
Transitional metal phosphide
CoP

ABSTRACT

Hydrogen evolution reaction (HER) and oxygen reduction reaction (ORR) have been considered as two critical processes in the field of electrocatalytic water-splitting for hydrogen production and fuel cells. However, the sluggish reaction kinetics of HER and ORR required efficient electrocatalyst such as Pt to promote such process. Transition metal phosphides (TMPs) exhibit great potential to replace noble metal electrocatalysts to accelerate HER and ORR due to their high activity and easy availability. Herein, a highly-efficient bifunctional CoP electrocatalyst for HER and ORR, featuring a unique core-shell structure decorated on nitrogen-doped carbon matrix was designed and constructed *via* etching a cobalt-based zeolitic imidazolate framework (ZIF-67) with phytic acid (PA) followed by pyrolysis treatment (PA-ZIF-67–900). Experimental results revealed that the pure-phase single-crystalline CoP exhibited outstanding electrocatalytic performance in HER and ORR, superior to $Co(PO_3)_2$ in PA-ZIF-67–700, hybrid phase of $Co(PO_3)_2$ and CoP in PA-ZIF-67–800 and Co_2P-doped CoP in PA-ZIF-67–1000. To reach the current density of 10 mA/cm^2 the as-synthesized CoP required an overpotential of 120 mV for HER in 1 mol/L KOH and half-wave potential of 0.85 V in O_2-saturated 0.1 mol/L KOH. This work present new clue for construction of efficient and bifunctional electrocatalyst in the field of energy conversion and storage

As energy and environmental problems become more and more serious [1–4], renewable energy conversion and storage technologies have become research hotspots [5,6]. Hydrogen as one of the clean, renewable, and cost-effective energy resources, has been considered to be promising alternative to fossil fuels [7,8], which can be accessed by electrocatalytic water-splitting [9,10]. On the other hand, zinc-air battery (ZAB) and direct methanol fuel cell (DMFC) serving as low-cost and environmentally friendly energy storage technique exhibits great application potential [11–13]. However, both hydrogen production and ZAB required efficient electrocatalysts to accelerate the sluggish reactions of hydrogen evolution reaction (HER) in water splitting process and oxygen reduction reaction (ORR) on the cathode of ZAB system. Until now, the state-of-the-art electrocatalyst for HER and ORR is Pt/C, but its large-scale application is prohibited due to its small reserves, high cost and poor stability [14]. Therefore, it is necessary to develop a low-cost and highly-efficient noble-metal-free electrocatalysts for HER and ORR.

Recently, transition metal phosphides (TMPs) such as FeP [15,16], CoP [17,18], NiP [19], have been reported as HER and ORR electrocatalysts [20,21]. Generally, the TMP-based catalysts were synthesized by wet chemical method using trioctylphosphine (TOP) [22] and triphenylphosphine (TPP) [23] or gas-solid reaction approach using NaH_2PO_2, PH_3 gas and red phosphorus as phosphorus sources [24–27]. Although the above-mentioned phosphating process has been widely developed, these phosphorus sources have certain toxicity and cause pollution to the environment, which greatly restricts their further utiliaztion. Therefore, pursuing a non-toxic and environment-benign phosphating process is meaningful and inevitable.

The cobalt-based zeolitic imidazolate framework (ZIF-67) is a metal-organic framework material with porous properties, high specific surface area and adjustable morphology [28,29]. Moreover, it can be pyrolyzed to form nitrogen-doped carbon substrate,

---

* Corresponding authors.
E-mail addresses: huangjf@sust.edu.cn (J. Huang), caoliyun@sust.edu.cn (L. Cao), fengyq@sust.edu.cn (Y. Feng).

https://doi.org/10.1016/j.cclet.2021.11.063

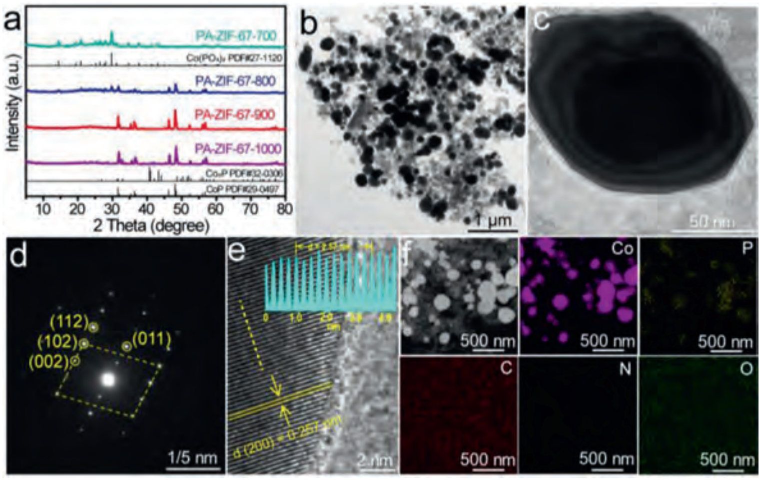

Fig. 1. Structure and morphology characterization of PA-ZIF-67–900. (a) XRD patterns of PA-ZIF-67–700, PA-ZIF-67–800, PA-ZIF-67–900 and PA-ZIF-67–1000. (b, c) TEM, (d) SAED, (e) HRTEM of PA-ZIF-67–900. (f) Corresponding elemental mapping for Co (purple), P (yellow), C (red), N (blue) and O (green) of PA-ZIF-67–900.

which is an ideal transition metal-based electrocatalyst precursor. In recent years, the ZIF-67 derived electrocatalysts have been widely reported [30,31], showing a very broad prospect owing to their low cost and high efficiency in water electrolysis and oxygen reduction. Phytic acid (PA) is a nontoxic and environmentally friendly compound, where the P–O bond can be broken to release P element as a source of phosphorus to form metallic phosphides [32]. Herein, we synthesized phase-mediated cobalt phosphides via etching a ZIF-67 with PA followed by pyrolysis treatment under H_2/Ar atmosphere (Figs. S1-S4 in Supporting information). Electrochemical measurement revealed that the pure phase CoP prepared at 900 °C (denoted as PA-ZIF-67–900) exhibits the most excellent HER and ORR catalytic performance and robust stability. This work presents a new clue for construction of efficient bifunctional TMP-based electrocatalyst in the field of energy storage and conversion.

The phase structure of PA-ZIF-67–900 was characterized by powder X-ray diffraction (XRD) along with its counterparts annealed at 700, 800 and 1000 °C, respectively. As shown in Fig. 1a, PA-ZIF-67–900 displayed diffraction peaks at 31.6°, 35.3°, 36.3°, 46.2°, 48.1°, 52.3°, 56.1° and 56.8°, definitely corresponding to the pure phase CoP (JCPDS No. 29–0497). Whereas the XRD pattern of PA-ZIF-67–700 can be assigned to pure phase $Co(PO_3)_2$ (JCPDS No. 27–1120), and PA-ZIF-67–800 is a hybrid phase of $Co(PO_3)_2$ and CoP. For PA-ZIF-67–1000, beside the dominant phase of CoP, a small amount of Co_2P miscellaneous phase was also observed. Raman spectroscopy was used to investigate the graphitization of the PA-ZIF-67–900. As shown in Fig. S5 (Supporting information), the ratio of D band (1345 cm^{-1}) and G band (1580 cm^{-1}) of PA-ZIF-67–900 (0.99) was similar to that of PA-ZIF-67–1000 (1.00), and higher than those of PA-ZIF-67–700 (0.90) and PA-ZIF-67–800 (0.93). The higher graphitization of PA-ZIF-67–900 could facilitate the charge transfer during the electrocatalytic process.

The morphology of PA-ZIF-67–900 was then investigated by scanning electron microscopy (SEM) and transmission electron microscopy (TEM). From Fig. 1b and Fig. S6a (Supporting information), it can be seen that in PA-ZIF-67–900 there exist plenty of nanoparticles with average size of 100–200 nm distributed on the surface of carbon matrix. A closer inspection of the nanoparticle (Fig. 1c) disclosed an architecture of PA-ZIF-67–900 with a core enveloped with multiple shells. In order to further prove the multilayer core-shell structure, high-resolution TEM (HRTEM) characterization was carried out, as shown in Fig. S6b, the structure of carbon layer@CoP@carbon layer@CoP was observed. Selected area electron diffraction (SAED) pattern (Fig. 1d) of a single PA-ZIF-67–900 particle exhibited regular spots corresponding to (110), (002), (102), and (112) crystal planes of the single-crystalline orthorhombic CoP, which is in good agreement with the XRD result. HRTEM image (Fig. 1e) displayed a lattice fringe of 0.257 nm [33,34], which matched well with the (002) crystal plane of CoP. Besides, the element mapping (Fig. 1f) unveiled that the CoP nanoparticles were decorated on the nitrogen-doped carbon matrix. It was worth noting that the pyrolysis temperature is vital to form core and multi-shell structure. When the temperature is very low, *i.e.*, 700 °C, only large blocks were obtained (Fig. S7 in Supporting information); while at 800 °C nanoparticles featuring a solid core wrapped with one-layer carbon shell imbedded onto the surface of carbon substrate was observed (Fig. S8 in Supporting information). The PA-ZIF-67–1000 possessed nanoparticles with irregular shape and nonuniform size (Fig. S9 in Supporting information), which may be attributed to the heterogenous phase in PA-ZIF-67–1000.

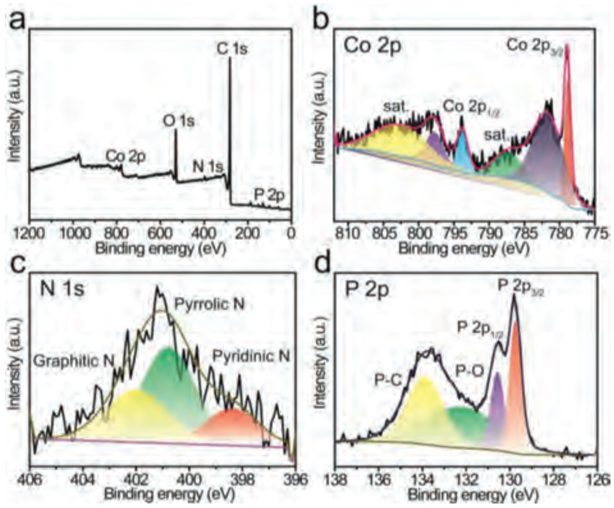

Fig. 2. XPS spectrum of PA-ZIF-67–900. (a) XPS survey spectrum, (b) Co 2p, (c) N 1s and (d) P 2p high resolution spectrum of PA-ZIF-67–900.

The chemical state and electronic structure of PA-ZIF-67–900 were evaluated by X-ray photoelectron spectroscopy (XPS). Fig. 2a presents the XPS survey spectrum of PA-ZIF-67–900, indicating the existence of Co, P, C, N and O in PA-ZIF-67–900. The high-resolution Co 2p spectrum could be deconvoluted into three

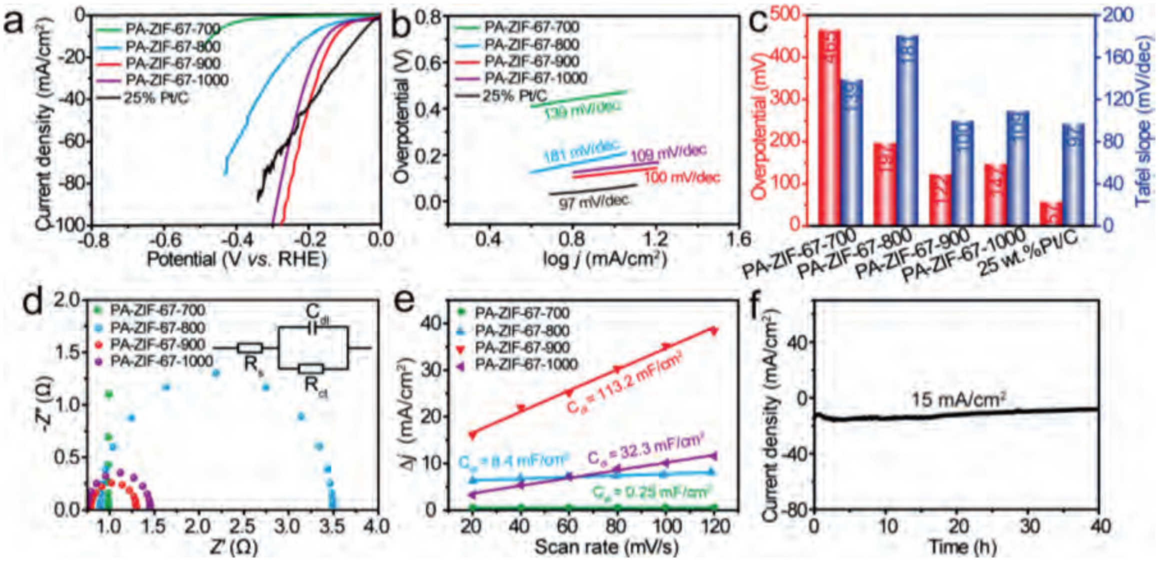

Fig. 3. HER performance of PA-ZIF-67–900. (a) Polarized LSV curves, (b) Tafel slope, (c) comparison of overpotential at 10 mA/cm^2 (red column) and Tafel slope (blue column) for PA-ZIF-67–700 (green), PA-ZIF-67–800 (blue), PA-ZIF-67–900 (red), PA-ZIF-67–1000 (purple) and 25% Pt/C (black). (d) Nyquist plots and (e) current density difference against scan rate of PA-ZIF-67–700 (green), PA-ZIF-67–800 (blue), PA-ZIF-67–900 (red) and PA-ZIF-67–1000 (purple). (f) Chronoamperometric current-time curve of PA-ZIF-67–900.

groups as displayed in Fig. 2b. Two distinct peaks at binding energy of 778.88 and 793.77 eV were attributed to Co $2p_{3/2}$ and Co $2p_{1/2}$, respectively, corresponding to the Co–P bond in cobalt phosphide [20]. The peaks at 781.64 and 797.69 eV can be assigned to oxidized cobalt species, which was ascribed to surface oxidation of PA-ZIF-67–900, and the peaks at 787.25 and 802.51 eV are satellite [20]. Moreover, the N 1s spectrum exhibited three peaks located at 398.38, 400.79 and 401.97 eV (Fig. 2c), which can be assigned to pyridinic N, pyrrolic N and graphitic N, respectively [35,36]. It has been established that pyridinic N and graphitic N can promote the catalytic ORR activity [37], and the pyrrolic N at the edge of the carbon plane has also been reported as the active site for HER process [38]. The electronegativity of N (3.04) is stronger than that of C (2.55), which polarizes the carbon matrix, enhancing the ability of carbon atoms nearby to capture oxygen during the ORR process [39,40]. In addition, the high-resolution XPS spectra of P 2p displayed binding energy at 129.76 and 130.56 eV of the $2p_{3/2}$ and $2p_{1/2}$, which agreed with the value in the literature for CoP (Fig. 2d) [41]. And the peak at 130.2 and 133.87 eV corresponds to oxidized P species [41]. Particularly, compared with the binding energy of metallic Co (778.1 eV) and elemental P (130.0 eV), the binding energy of Co $2p_{3/2}$ upshifts while the binding energy of P $2p_{3/2}$ downshifts, indicating that charge transfer occurs between P and Co to form CoP [42], which would facilitate the electrocatalytic process.

To further investigate the microscopic structure of PA-ZIF-67–900, nitrogen adsorption/desorption measurement was then carried out. The N_2 adsorption/desorption curves (Fig. S10 in Supporting information) displayed a type IV isotherm [32] with Brunauer-Emmett-Teller (BET) specific surface area of 292.41 m^2/g. Three peaks at 1.74, 3.99 and 32 nm in the pore size distribution diagram of PA-ZIF-67–900 are observed, indicating that PA-ZIF-67–900 has a microporous/mesoporous hierarchical pore structure which could facilitate the mass transportation during the electrocatalytic process [32].

The electrocatalytic HER performance of PA-ZIF-67–900 was evaluated using a standard three-electrode system in 1 mol/L KOH at room temperature. For comparison, the HER activity of PA-ZIF-67–700, PA-ZIF-67–800, PA-ZIF-67–1000 and the commercial 25% Pt/C was also tested under the same condition. The linear sweep voltammetry (LSV) curves are shown in Fig. 3a. It can be seen that PA-ZIF-67–900 with a pure phase of CoP outperformed PA-ZIF-67–700, PA-ZIF-67–800 and PA-ZIF-67–1000, even 25% Pt/C at large current density. To reach the current density of 10 mA/cm^2, the PA-ZIF-67–900 required an overpotential of only 120 mV, which is lower than that of PA-ZIF-67–700 (465 mV), PA-ZIF-67–800 (197 mV) and PA-ZIF-1000 (147 mV) as shown in Fig. 3c. The HER reaction kinetics was assessed by the Tafel slope derived from the LSV curves. As shown in Fig. 3b, the Tafel slopes of PA-ZIF-67–900, PA-ZIF-67–700, PA-ZIF-67–800, PA-ZIF-67–1000 and 25% Pt/C were 100, 139, 181, 109 and 97 mV/dec, revealing a fast kinetics of PA-ZIF-67–900 comparable to Pt/C following the Volmer–Heyrovsky mechanism [41]. Fig. 3d depicted the electrochemical impedance spectroscopy (EIS) curves. From the Nyquist plots it was indicated that PA-ZIF-67–900 shows a smaller semicircle diameter, suggesting a favorable charge transfer resistance of PA-ZIF-67–900 (0.5 Ω) compared to PA-ZIF-67–700 (147.7 Ω), PA-ZIF-67–800 (3.1 Ω) and PA-ZIF-67–1000 (0.7 Ω). Moreover, the electrochemical double-layer capacitance (C_{dl}) obtained by the cyclic voltammetry (CV) measurement was used to assess the active reaction sites, which was proportional to the electrochemical active surface area (ECSA) [43]. As illustrated in Fig. 3e, PA-ZIF-67–900 exhibited a higher C_{dl} value (113.2 mF/cm^2) than that of PA-ZIF-67–700 (0.25 mF/cm^2), PA-ZIF-67–800 (8.4 mF/cm^2) and PA-ZIF-67–1000 (32.3 mF/cm^2), indicating that PA-ZIF-67–900 has the largest amount of electrochemically active sites. These results demonstrated that the pure-phase single-crystalline CoP in PA-ZIF-67–900 possessed a much enhanced HER activity compared to the $Co(PO_3)_2$ in PA-ZIF-67–700, hybrid phase of $Co(PO_3)_2$ and CoP in PA-ZIF-67–800 and Co_2P-doped CoP in PA-ZIF-67–1000. In addition, the HER catalytic stability of PA-ZIF-67–900 was investigated by the chronoamperometric test. As can be seen from Fig. 3f, the catalytic performance of PA-ZIF-67–900 maintained stable for at least 40 h. To explore the structural stability of the catalyst, the TEM of PA-ZIF-67–900 after chronoamperometric current-time measurement for HER was performed, as shown in Fig. S11 (Supporting information), the core-shell structure can still be observed. Notably, the HER performance of PA-ZIF-67–900 is superior to many other recently-reported CoP-based electrocatalysts in alkaline medium (Table S1 in Supporting information).

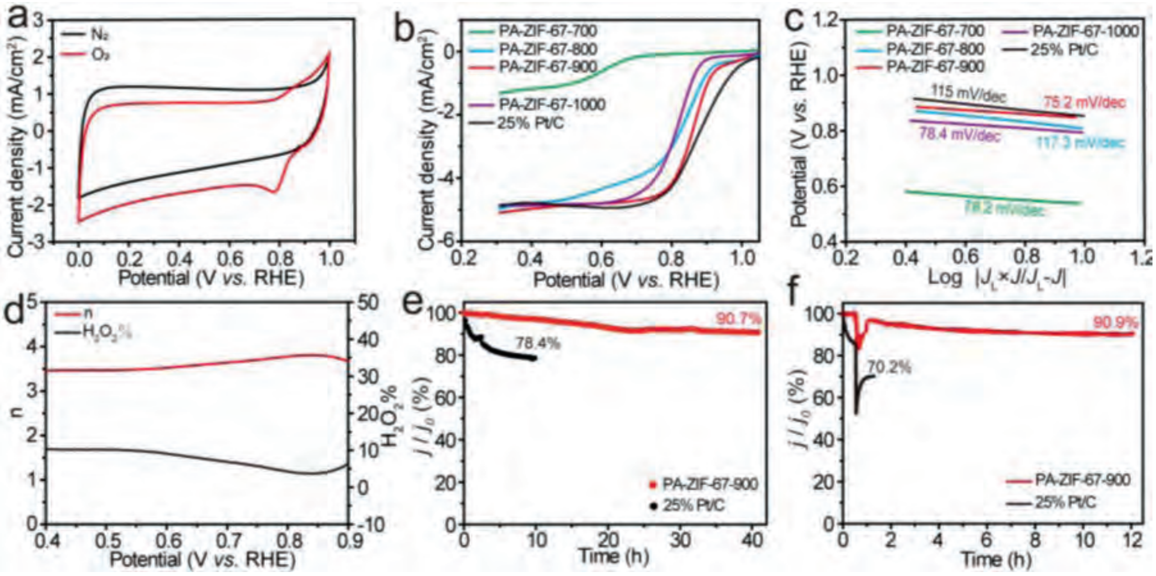

Fig. 4. ORR performance of PA-ZIF-67–900. (a) CV curves of PA-ZIF-67–900 in the presence of N_2 (black) and O_2 (red). (b) LSV curves and (c) Tafel slope for PA-ZIF-67–700 (green), PA-ZIF-67–800 (blue), PA-ZIF-67–900 (red), PA-ZIF-67–1000 (purple) and 25% Pt/C (black). (d) Number of electron transfer (left) and H_2O_2 yield (right) of PA-ZIF-67–900. (e) Normalized current density (j/j_0) against time plot and (f) methanol tolerance test of PA-ZIF-67–900 (red) and 25% Pt/C (black).

The ORR performance of the as-synthesized PA-ZIF-67–900 along with the reference electrocatalysts was evaluated in 0.1 mol/L KOH using a rotating disk electrode (RDE). Fig. 4a describes the CV curves of PA-ZIF-67–900 in the presence and absence of O_2 atmosphere with a scan rate of 50 mV/s. It can be seen that a sharp peak appeared at 0.78 V (*vs*. RHE) in the CV curve of O_2-saturated 0.1 mol/L KOH in contrast to the case of N_2-saturated 0.1 mol/L KOH, indicating the efficient ORR activity of PA-ZIF-67–900. The LSV curves of a series of electrocatalysts measured at 1600 rpm in O_2-saturated 0.1 mol/L KOH is shown in Fig. 4b. The PA-ZIF-67–900 with pure-phase CoP exhibited a half-wave potential ($E_{1/2}$) of 0.85 V and limiting current density (J_L) of 5 mA/cm^2, which is comparable to that of 25% Pt/C ($E_{1/2} = 0.86$ V and $J_L = 5$ mA/cm^2), and outperforms the other three electrocatalysts with phosphate or hybrid phases. Moreover, the ORR performance of PA-ZIF-67–900 are competitive to many other CoP-based electrocatalysts in alkaline media (Table S2 in Supporting information). The corresponding Tafel slope (Fig. 4c) of PA-ZIF-67–900 is 75.2 mV/dec, which is lower than that of 25% Pt/C (115 mV/dec), PA-ZIF-67–700 (78.2 mV/dec), PA-ZIF-67–800 (117.3 mV/dec) and PA-ZIF-1000 (78.4 mV/dec), indicating a favorable reaction kinetics of PA-ZIF-67–900 for ORR performance. The number of transferred electrons (n) and H_2O_2 yield (H_2O_2%) in the ORR process of PA-ZIF-67–900 were evaluated at 1600 rpm by rotating ring-disk electrode (RRDE) measurement. As shown in Fig. 4d, the n value of PA-ZIF-67–900 is in the range of 3.5–3.8 and H_2O_2 yield is lower than 10%, indicating that the PA-ZIF-67–900 could efficiently reduce oxygen *via* a four-electron reaction route in alkaline medium. In order to evaluate the catalytic stability of the electrocatalysts, a chronoamperometric response at 0.6 V was tested. As shown in Fig. 4e, after 40 h continuous operation, the catalytic activity of PA-ZIF-67–900 still maintained 90.7% of the initial, however, it decayed to 78.4% for 25% Pt/C only after 10 h, demonstrating the robust catalytic durability of PA-ZIF-67–900. In addition, the methanol tolerance is an important indicator to evaluate the ORR electrocatalyst for DMFC because the methanol can poison the electrocatalyst. As displayed in Fig. 4f, PA-ZIF-67–900 exhibits an excellent tolerance against methanol relative to 25% Pt/C. After injection with 3 mol/L methanol into the electrolyte, the activity of PA-ZIF-67–900 can recover to 90.9% while 25% Pt/C is only 70.2%. In order to explore the catalytic mechanism of ORR, the XPS and TEM of PA-ZIF-67–900 after the chronoamperometric response were characterized. As shown in Fig. S12 (Supporting information), the peak for Co $2p_{3/2}$ after stability test positively shifted to 780.25 eV. Meanwhile P was also oxidized after electrolysis. And from Fig. S13 (Supporting information), the core-shell structure of PA-ZIF-67–900 is retained.

In summary, a multilayer CoP core-shell structure decorated on N-doped carbon substrate as a highly efficient and stable HER and ORR bifunctional electrocatalyst was designed and synthesized. The results demonstrated that the pure-phase single-crystalline CoP (PA-ZIF-67–900) exhibited outstanding electrocatalytic performance in HER and ORR, superior to $Co(PO_3)_2$ in PA-ZIF-67–700, hybrid phase of $Co(PO_3)_2$ and CoP in PA-ZIF-67–800 and Co_2P-doped CoP in PA-ZIF-67–1000. For example, the pure-phase CoP formed at 900 °C shows the most efficient HER and ORR performance, achieving the current density of 10 mA/cm^2 with an overpotential of 120 mV for HER in 1 mol/L KOH and half-wave potential of 0.85 V in O_2-saturated 0.1 mol/L KOH. Besides, the PA-ZIF-67–900 displayed a desirable long-term catalytic stability and methanol tolerance, indicating its potential application in water splitting, ZAB and DMFC devices. The present work provides a new platform for construction of efficient and bifunctional electrocatalyst in the field of energy conversion and storage.

Declaration of competing interest

The authors declare that they have no known competing financial interests or personal relationships that could have appeared to influence the work reported in this paper.

Acknowledgments

Authors thank to Shaanxi Key Laboratory of Green Preparation and Functionalization for Inorganic Materials for their experimental platform and testing conditions. This work was supported by the National Natural Science Foundation of China (Nos. 52073166, 52072226), the Xi'an Key Laboratory of Green Manufacture of Ceramic Materials Foundation (No. 2019220214SYS017CG039), the Key Program for International S&T Cooperation Projects of Shaanxi Province (Nos. 2020KW-038, 2020GHJD-04), Science and Technology Program of Xi'an, China (No. 2020KJRC0009) and Scientific Research Program Funded by Shaanxi Provincial Education Department (No. 20JY001), Science and Technology Resource Sharing Platform of Shaanxi Province (No. 2020PT-022), Science and Technology Plan of Weiyang District, Xi'an (No. 202009). Dr. Y. Q. Feng is grateful for the support from the Science and Technology Youth Stars Project of Shaanxi Province (No. 2021KJXX-35).

Supplementary materials

Supplementary material associated with this article can be found, in the online version, at doi:10.1016/j.cclet.2021.11.063.

References

[1] Y. Feng, P. Dong, L. Cao, J. Mater. Chem. A 9 (2021) 2135–2144.
[2] L. Fu, R. Wang, C. Zhao, Chem. Eng. J. 414 (2021) 128857.
[3] H. Yang, C. He, L. Fu, Chin. Chem. Lett. 32 (2021) 3202–3206.
[4] R. Wang, C. He, W. Chen, Chin. Chem. Lett. 32 (2021) 3821–3824.
[5] Y. Feng, X. Wang, J. Huang, Chem. Eng. J. 390 (2020) 124525.
[6] L. Ling, Q. Ma, Y. Yu, B. Zhang, Trans. Tianjin Univ. 27 (2020) 180.
[7] D. He, L. Cao, J. Huang, J. Energy Chem. 47 (2020) 263–271.
[8] W. Du, Y. Shi, W. Zhou, Angew. Chem. Int. Ed. 60 (2020) 7051–7055.
[9] S. Zhou, H. Jang, Q. Qin, Chem. Eng. J. 414 (2021) 128865.
[10] Y. Guo, T. Park, J. Yi, Adv. Mater. 31 (2019) 1807134.
[11] E. Vijayakumar, S. Ramakrishnan, C. Sathiskumar, Chem. Eng. J. 428 (2022) 131115.
[12] R. Hao, J. Chen, Z. Wang, J. Colloid Interface Sci. 586 (2021) 621–629.
[13] D. Wang, P. Yang, H. Xu, J. Power Sources 485 (2021) 229339.
[14] H. Yang, Y. Zhang, F. Hu, Nano Lett. 15 (2015) 7616–7620.
[15] D. Zeng, T. Zhou, W. Ong, ACS Appl. Mater. Interfaces 11 (2019) 5651–5660.
[16] F. Ma, C. Xu, F. Lyu, Adv. Sci. 6 (2019) 1801490.
[17] D. Zhu, L. Wang, M. Qiao, Chem. Commun. 56 (2020) 7159–7162.
[18] Y. Lai, W. Xia, J. Li, Electrochim. Acta 375 (2021) 137966.
[19] B. Hui, K. Zhang, Y. Xia, Electrochim. Acta 330 (2020) 135274.
[20] L. Ji, J. Wang, X. Teng, ACS Catal. 10 (2019) 412–419.
[21] H. Du, R. Kong, X. Guo, Nanoscale 10 (2018) 21617–21624.
[22] Y. Pan, Y. Lin, Y. Chen, J. Mater. Chem. A 4 (2016) 4745–4754.
[23] Z. Huang, Z. Chen, Z. Chen, Nano Energy 9 (2014) 373–382.
[24] C. Han, T. Zhang, Q. Cai, J. Am. Ceram. Soc. 102 (2019) 5484–5493.
[25] S.V. Mohite, R. Xing, B. Li, Inorg. Chem. 59 (2020) 1996–2004.
[26] A. Dutta, A.K. Samantara, S.K. Dutta, ACS Energy Lett. 1 (2016) 169–174.
[27] Z. Liu, J. Wang, C. Zhan, J. Mater. Sci. Technol. 46 (2020) 177–184.
[28] Z. Chen, Y. Ha, H. Jia, Adv. Energy Mater. 9 (2019) 1803918.
[29] J. Li, X. Wang, G. Zhao, Chem. Soc. Rev. 47 (2018) 2322.
[30] J. Shi, F. Qiu, W. Yuan, Chem. Eng. J. 403 (2021) 126312.
[31] L. Chai, Z. Hu, X. Wang, Adv. Sci. 7 (2020) 1903195.
[32] X. Wang, Z. Na, D. Yin, ACS Nano 12 (2018) 12238–12246.
[33] G. Liu, M. Wang, Y. Xu, J. Power Sources 486 (2021) 229351.
[34] Y. Zhang, Y. Wang, T. Wang, Adv. Mater. Interfaces 7 (2019) 1901302.
[35] Y. Cao, H. Lu, B. Xu, Chem. Eng. J. 378 (2019) 122247.
[36] S. Li, S. Yang, Y. Wang, Carbon 59 (2013) 418–429.
[37] X. Han, W. Zhang, X. Ma, Adv. Mater. 31 (2019) 1808281.
[38] K. Artyushkova, A. Serov, S. Rojas-Carbonell, J. Phys. Chem. C 119 (2015) 25917–25928.
[39] C.H. Choi, S.H. Park, S.L. Woo, ACS Nano 6 (2012) 7084–7091.
[40] K. Gong, F. Du, Z. Xia, Science 323 (2009) 760–764.
[41] J. Liu, C. Zhang, S. Yuan, Chem. Eng. J. 428 (2022) 131326.
[42] Y. Pan, K. Sun, S. Liu, J. Am. Chem. Soc. 140 (2018) 2610–2618.
[43] Q. Hu, G. Li, X. Huang, J. Mater. Chem. A 7 (2019) 19531–19538.